PHYSICAL PARAMETERS OF STANDARD AND BLOWOUT JETS

Stefano Pucci[1], Giannina Poletto[2], Alphonse C. Sterling[3], and Marco Romoli[1]
[1] Department of Physics and Astronomy, University of Firenze, I-50121 Firenze, Italy; stpucci@arcetri.astro.it
[2] INAF–Arcetri Astrophysical Observatory, I-50125 Firenze, Italy
[3] Space Science Office, NASA/MSFC, Huntsville, Al 35812, USA

ABSTRACT

The X-ray Telescope on board the *Hinode* mission revealed the occurrence, in polar coronal holes, of much more numerous jets than previously indicated by the *Yohkoh*/Soft X-ray Telescope. These plasma ejections can be of two types, depending on whether they fit the standard reconnection scenario for coronal jets or if they include a blowout-like eruption. In this work, we analyze two jets, one standard and one blowout, that have been observed by the *Hinode* and *STEREO* experiments. We aim to infer differences in the physical parameters that correspond to the different morphologies of the events. To this end, we adopt spectroscopic techniques and determine the profiles of the plasma temperature, density, and outflow speed versus time and position along the jets. The blowout jet has a higher outflow speed, a marginally higher temperature, and is rooted in a stronger magnetic field region than the standard event. Our data provide evidence for recursively occurring reconnection episodes within both the standard and the blowout jet, pointing either to bursty reconnection or to reconnection occurring at different locations over the jet lifetimes. We make a crude estimate of the energy budget of the two jets and show how energy is partitioned among different forms. Also, we show that the magnetic energy that feeds the blowout jet is a factor of 10 higher than the magnetic energy that fuels the standard event.

Key words: Sun: activity – Sun: corona – Sun: flares – Sun: X-rays, gamma rays – techniques: spectroscopic

Online-only material: color figures

1. INTRODUCTION

The *Hinode*/X-ray Telescope (XRT) telescope, due to its higher spatial and temporal resolution and its wide temperature coverage (Kano et al. 2004; Golub et al. 2007), detected a larger number of X-ray jets in polar coronal holes (CHs) than expected on the basis of previous *Yohkoh* observations (Cirtain et al. 2007). This result raised interest in these jets, with the prospect that they could be small-size, low-energy phenomena corresponding to classical flares; polar jets might contribute to the high speed solar wind emerging from polar holes. As far as their similarity to large scale events, Moore et al. (2010, 2013) presented evidence that jets come in two different kinds, where about half of them are "standard" events that fit the standard reconnection scenario between emerging flux and open unipolar fields and the other half are "blowout" jets that result from the eruption of a magnetic arch along with the ejection of plasma in a process that may be a miniature version of what happens in major coronal mass ejection (CME) events.

The overall characteristics of jets, including their size, frequency, and duration, have been examined by, e.g., Savcheva et al. (2007), while their physical properties have been described by several authors who, however, did not differentiate between the two proposed categories of jets. The outflow speed of jets has been studied by, e.g., Kim et al. (2007), on the basis of *Hinode*/Extreme-ultraviolet Imaging Spectrometer (EIS) data. Culhane et al. (2007) used the same kind of data to study the temperatures and outflow speed of two jets; the light curves of the jets showed a post-jet enhancement in the cooler lines. The authors accordingly suggested that plasma was falling back to the Sun, and hence that the jets did not reach the outer corona. Nisticò et al. (2011) built temperature maps of jets observed by the Extreme Ultraviolet Imager (EUVI) and the Corona-graph1 (COR1) telescope on the SECCHI package (Howard

et al. 2008) on board the *STEREO* (Kaiser et al. 2008) mission; they used the 195 Å to 171 Å filter ratio technique to investigate the thermal evolution of the observed events. The temperatures inferred from *Hinode*/EIS and *STEREO*/SECCHI did not completely agree: Culhane et al. (2007) give values ranging between 0.4 and 5 MK, while Nisticò et al. (2011) find values ranging between 0.8 and 1.3 MK. Whether this difference originates from the inadequacy of the single-ratio technique to describe the jet temperatures fully or whether there are differences between jets reaching high in the corona and jets falling back to the Sun is not clear. In another work that also did not specify the type of jet being analyzed, Doschek et al. (2010) observed one jet with *Hinode*/EIS and concluded that plasma within the jet had a temperature around 1.4 MK. Also, Madjarska (2011) performed a thorough analysis of a jet observed with *SOHO*/SUMER, *Hinode*/XRT, EIS, and *STEREO*/SECCHI EUVI *A* and *B* instrumentation, and found temperatures as high as 12 MK at the jet footpoint, while the outflowing plasma had temperatures ranging between 0.5 and 2 MK. On the other hand, blowout events have been recently studied, mainly using data from the Atmospheric Imaging Assembly (AIA; Lemen et al. 2011) instrument on board the *Solar Dynamics Observatory* (*SDO*) mission. Morton et al. (2012) and Shen et al. (2012) used these data and focused, respectively, on the quasi-periodic phenomena associated with these kinds of ejections and observations of the bubble-like and jet-like CMEs associated with the blowout event. Shen et al. (2012) aimed at understanding the mechanism giving rise to blowout jets and identifying their accompanying features, rather than deriving their physical parameters.

In this work, we analyze two ejections, whose characteristics comply with the properties of either standard jets or blowout jets. We determine their temperatures, densities, and outflow speeds in order to investigate whether the two jet types have different
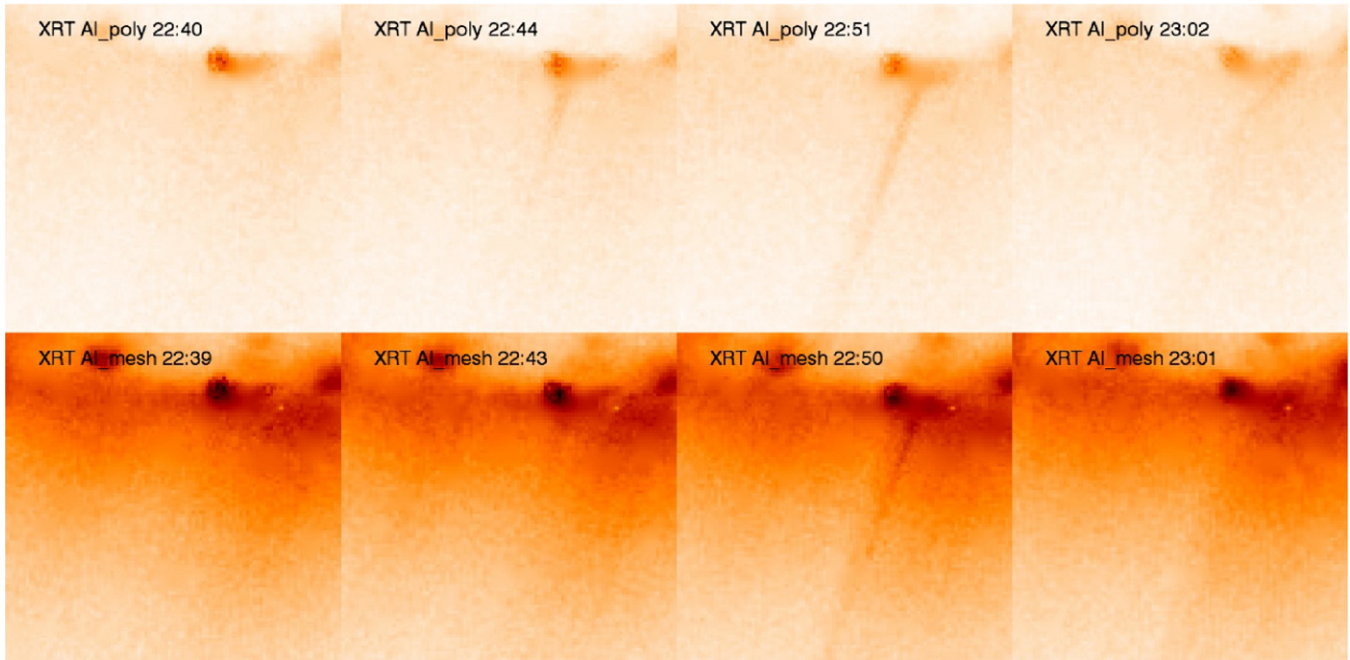
Figure 1. Evolution of the standard jet, as observed in the *Hinode*/XRT *Al_poly* (top row) and *Al_mesh* (bottom row) filters, on 2008 July 1. The first panel on the left (top and bottom rows) shows the pre-jet corona.

(A color version of this figure is available in the online journal.)

physical parameters. We also calculate the temporal profiles of these quantities and their profile along the jet structures. Using the estimates obtained for physical parameters of the events allows us to make a crude evaluation of the energy budget of standard versus blowout ejection and to put some constraints on the magnetic field energy release that fueled the jets. This paper is organized as follows. In Section 2, we describe the data sets used in our analysis and the properties of the jets we examined. In Section 3, we illustrate the spectroscopic techniques by which we inferred the jet physical parameters. Section 4 gives results. In Sections 5 and 6, we conclude by giving a crude estimate of the jets' energy budgets, and then compare our results with predictions from theoretical models.

2. OBSERVATIONS

We have selected two prominent events that are well-observed and are good representatives of the two jet types. As both events are limb events, we are able to minimize problems associated with isolating the jet emission from the contribution of the foreground and background corona.

As a good example of a standard jet, we selected an event, rooted in the southern polar CH at 115 arcsec E, 970 arcsec S (as seen by *Hinode*/XRT), that started at 22:44 UT on 2008 July 1 and lasted ≈20 minutes. *Hinode*/XRT images of the jet (Figure 1) show that it has the typical features of a standard jet: an X-ray flaring bright point (BP) located off to the side of the jet and a jet spire that migrates in a direction away from the BP with time over the event's lifetime. These properties agree with the predictions of the standard model from Shibata et al. (1992), where the jet occurs as a consequence of reconnection between the emerging flux and the unipolar ambient fields. The jet and the associated BP were also observed by *STEREO B*, while they fall outside the *STEREO A* field of view (FOV); the two spacecraft at that time were separated by ≈59°.

Over the jet lifetime, the *Hinode*/XRT telescope obtained data in three different filters: *C_poly*, *Al_poly*, and *Al_mesh*, with

a cadence of about 110 s, a plate scale of 1.0 arcsec pixel^{-1}, and exposure times of 33, 12, and 23 s, respectively. The response functions of these filters (together with filter ratios) can be found in Narukage et al. (2011). The EUVI instruments on board the *STEREO B* satellite acquired images in four different narrowband filters with a plate scale of 1.6 arcsec pixel^{-1}. The first filter was the 17.1 nm waveband (which includes Fe IX and Fe X lines with a peak sensitivity for plasma at 1.3×10^6 K), with an average cadence of ≈150 s and exposure times of either 16 s or 4 s. The second filter was the 19.5 nm waveband (which includes lines from the Fe XII and Fe XXIV ions and is most sensitive to plasma at $T = 1.5 \times 10^6$ K), with a cadence of 600 s and an exposure time of 16 s. The third filter was the 28.4 nm waveband (which includes the Fe XV line at 284 Å and is most sensitive to plasma at 2×10^6 K), with a 1200 s cadence and a 32 s exposure time. The fourth filter was the 30.4 nm waveband (which is dominated by the He II line and has its peak sensitivity at ≈6–8 $\times 10^4$ K), with a cadence of 600 s and an exposure time of 4 s. The response functions of these filters as a function of temperature are given in Wuelser et al. (2004) and Howard et al. (2008).

The blowout jet occurred on 2007 November 3 at ⩽11:53 UT, in the northern polar CH, at 170 arcsec W, 950 arcsec N, as seen by *Hinode*/XRT, and had a duration of about 30 minutes. *Hinode*/XRT took data only in the *Al_poly* filter, acquiring images with a 40 s cadence and an exposure time of 16 s. Figure 2 shows a sequence of XRT images from this event that display the typical characteristics of a blowout jet, such as the X-ray flaring of the whole base arcade, the blowout eruption of the core field, and the extra jet strands rooted at different locations within the flaring BP. Further evidence for classifying this event as a blowout is given in Section 4.2.

Observations of the jet and the associated BP have also been acquired by both *STEREO* spacecraft (separation ≈40°). The cadence and exposure times for both EUVI *A* and *B* are, in the 171, 195, 284, and 304 Å wavebands, respectively, 150 and 4 s, 600 and 16 s, 1200 and 32 s, and 600 and 4 s. By comparing
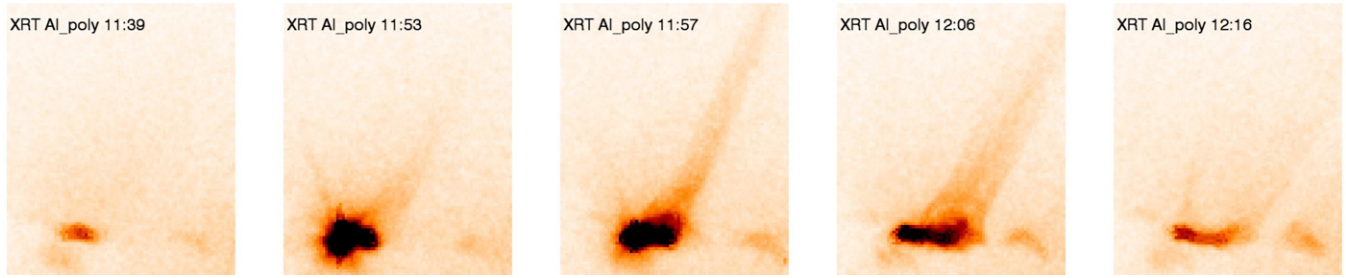
Figure 2. *Hinode*/XRT *Al_poly* images of the evolution of the blowout jet, which occurred on 2007 November 3. The left panel shows the pre-jet corona. There are no images closer in time to the jet initiation because of a 15 minutes gap in the *Hinode* data.

(A color version of this figure is available in the online journal.)

simultaneous images of the jet acquired by *STEREO A and B*[4] in the 171 Å EUVI channel, we can reconstruct its three-dimensional structure at a given time. This procedure is especially useful in considering the possibility that we could be observing a "magnetic twist jet," produced by reconnection between twisted and untwisted flux tubes; such jets were suggested twenty years ago by Shibata et al. (1992) and one was indeed observed in *STEREO* data by Patsourakos et al. (2008) and modeled, e.g., by Pariat et al. (2009). Emergence of a twisted flux rope might relatively easily result in a blowout jet where the base arch erupts. Indeed, *SDO*/AIA have recently provided evidence of blowout jets and untwisting fields (Morton et al. 2012; Chen et al. 2012).

In Figure 3, the left panels show one strand of the blowout jet (see Section 4.2), as observed by EUVI *B* in the 171 Å channel at 12:01 UT (upper panel) and at 12:06 UT (lower panel). The right panels show the three-dimensional reconstruction obtained by comparing the EUVI *B* 171 Å images with the corresponding simultaneous[4] images from EUVI *A* using the *scc_measure* routine of the Solar SoftWare (SSW) package. While the three-dimensional reconstruction at 12:01 UT shows clearly that the jet strand is, at that time, characterized by a twisted magnetic line, at 12:06 UT the reconstruction presents evidence for an untwisting of the flux tube.

Another telescope that might provide relevant information about the events is the COR1 coronagraph on board the *STEREO* missions, which acquires images with a cadence of 5 minutes over a FOV that extends from 1.4 to 4 solar radii. Detecting the jet in the COR1 FOV implies the jets reach high enough to possibly escape into the heliosphere. We will examine this idea in Sections 4.1 and 4.2.

3. DATA ANALYSIS

XRT and EUVI multi-filter data of the standard and blowout jets, respectively, allow us to measure the temperature and the electron density of the jet plasma via the "filter-ratio method." Filters on the XRT and EUVI telescopes are characterized by a response that depends on temperature, F_{fil} (usually given as DN s^{-1} pixel^{-1} for a unit column emission measure (CEM, cm^{-5})), where "DN" stands for data number. The measured intensity I_{fil} in a given filter can be written as

$$I_{fil} = F_{fil}(T) \int n_e^2 dl, \qquad (1)$$

which shows that the measured intensities (in DN s^{-1} pixel^{-1}) depend on the filter response, which is in turn a function of temperature; this filter response also depends on the abundance of the element whose lines enter the temperature regime probed by the filter. The intensity also depends on the plasma CEM ($n_e^2 l$), where we assumed $n_e = n_i$ and l is the depth of the emitting region along the line of sight (LOS). If the intensity of lines formed at temperature T_{line} is measured by two different filters, the ratio of the measured intensities gives the temperature of the plasma where the lines form, provided that they originate within the same region, and hence have the same CEM.

While the filter-ratio method is quite simple in principle, it conceals problems not immediately obvious. For instance, the same value of the filter ratio may correspond to a number of different temperatures. Furthermore, the emitting plasma may not be isothermal, which is a quite serious problem that may be overcome somewhat by using multiple filter ratios. Additional difficulties arise when we need to find the temperature of a feature embedded in a region whose contribution has to be separately identified before finding the temperature of the confined structure; for example, for a jet, this fact means subtracting the contribution of the foreground and background corona that add to the jet LOS emission.

We now describe how we inferred jet temperatures via the filter-ratio technique. As a first step, *Hinode* and EUVI images were calibrated via the SSW *xrt_prep* and *euvi_prep* routines to obtain calibrated images normalized to the exposure time. We then selected an image at a time prior to, but as close as possible to, the time of the jet initiation, to be used as a background reference image. We then identified the jet in successive images, and a "mask" of fixed width and height was determined such that a significant part of the jet could fit in the box, including its maximum extension; the mask changes position with time, following the jet displacement discussed above, but maintains a fixed height and width. We completed this procedure for each wavelength that we used for the study.

The same mask was used to select an area of the same size and location in the background image; pixels within this area are representative of the CH emission and, possibly, the plumes that overlap the jet along the LOS. We then degraded the resolution of the XRT data, binning over 2 × 8 pixels (i.e., 2.1 × 8.2 arcsec) across and along the jet axis. Analogously, the EUVI data were degraded by binning over 2 × 2 pixels (3.2 × 3.2 arcsec). The binning across the jet was dictated by the width of the jet (2 arcsec), hence we ignored the transverse structure of the jet, while we selected the binning along the jet axis to provide a signal-to-noise ratio ⩾20. We adopted the same binning to infer the profile of intensity versus distance of the background over the positions later occupied by the jet. These
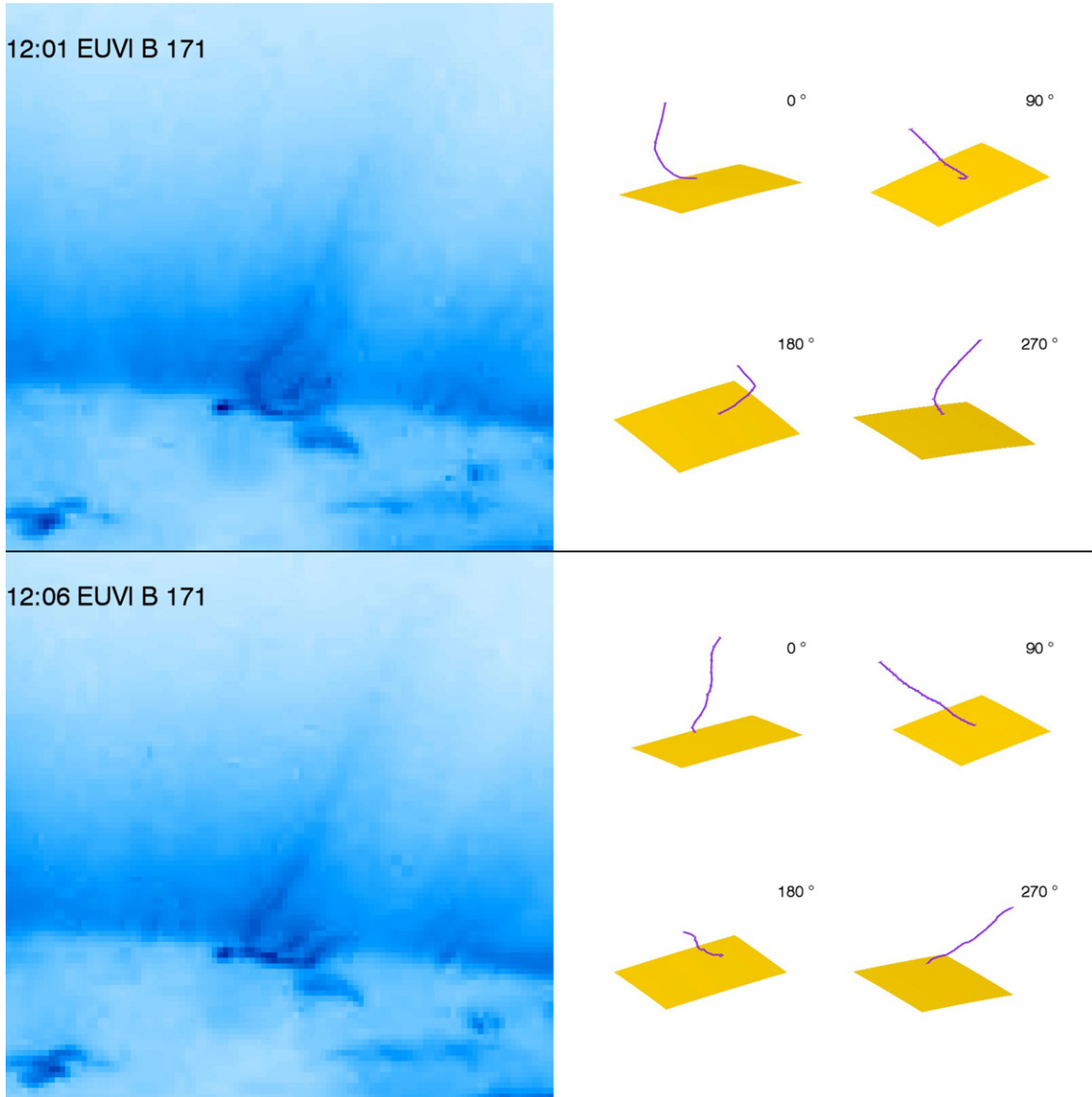
---

[4] We point out that simultaneous images of the Sun are acquired by the *STEREO A and B* instruments by imaging the Sun at slightly different times, depending on the distance of the two spacecraft from the Sun. For the jet on 2007 November 3, images were taken with a 43 s time separation. See http://stereo-ssc.nascom.nasa.gov/cgi-bin/make_where_gif.

Figure 3. Left panels: one strand of the blowout jet, as observed by EUVI *B* in the 171 Å channel at 12:01 UT (upper panel) and at 12:06 UT (lower panel). Right panels: the three-dimensional reconstruction at 12:01 and 12:06 UT of the strand from *STEREO*/EUVI *A* and *B* images in the 171 Å channel, indicating an untwisting of the flux tube (viewing angles in degrees).

(A color version of this figure is available in the online journal.)

degraded data have been used to build the profiles of intensity versus distance-along-the-jet axis that appear in Figures 4 and 8. The jet intensity profile has been fit with a fourth-order polynomial (to allow inhomogeneities, if any, to show up), while the background profile has been fit with a second-order polynomial, adequate to represent its behavior, as we assumed that the background intensity is constant over the duration of the jet. Because the jet intensity profile includes emission from the ambient corona, the jet emission has been isolated by subtracting the background intensity profile from the jet intensity profile. At each time, the maximum height reached by the jet is set to the height where the jet and background intensities differ by at least 2σ, where $\sigma = \sigma 1 + \sigma 2$ is the sum of the standard deviation of the background, $\sigma 1$, and the standard deviation of the jet, $\sigma 2$. The latter has been calculated assuming a Poisson distribution for the incoming photons. For the XRT data, we used the SSW routine xrt_cvfact to obtain the temperature-dependent conversion

factor $K^{(1)}$ between the measured DN and the incoming photons N_{ph}:

$$N_{\mathrm{ph}} = \frac{\mathrm{DN}}{K^{(1)}(T)} \qquad (2)$$

(see Equation (10) in Narukage et al. 2011). Next, we followed the procedure of Narukage et al. (2011) to calculate the standard deviation of the filter ratios and temperatures.

The EUVI data are converted to photons by the calibration procedure. The error of the background intensity is given by the 1σ uncertainty in the adopted fit coefficients.

Once the jet intensity has been isolated, we take the ratio between the available filters. In particular, for XRT, we use the filter pairs Al_poly/Al_mesh and C_poly/Al_mesh, as these ratios are monotonic functions of temperature over the range expected in our analysis. For the EUVI data, we take the ratios the 195 Å/171 Å data and the 284 Å/195 Å data,
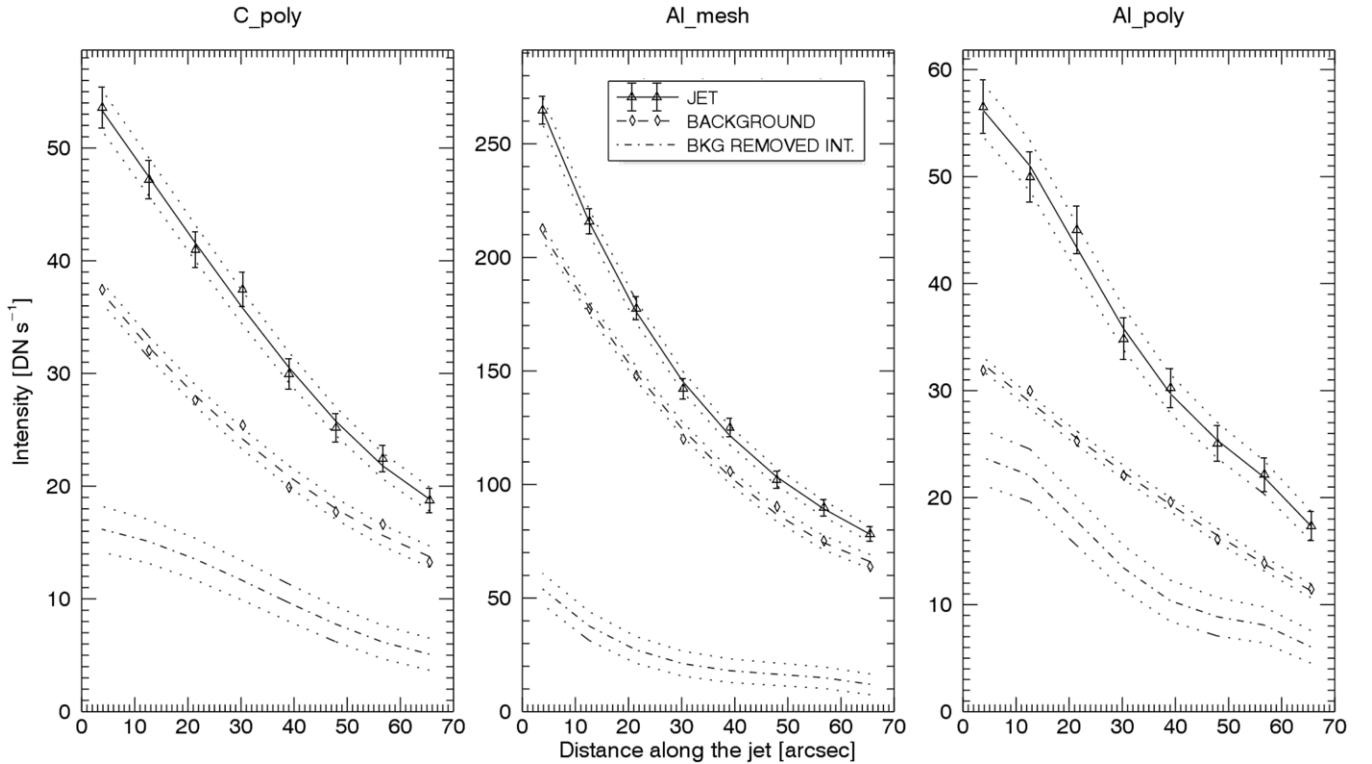
Figure 4. Measured values and fitted profiles of intensity vs. distance: along the standard jet with background (solid line and triangles), in the background (dashed line and diamonds), and along the standard jet after removing the background contribution (dash-dotted line). Data are taken in the XRT *C_poly* (left panel), *Al_mesh* (middle panel), and *Al_poly* (right panel) filters at ≈22:51 UT for the jet profile and at ≈22:30 UT for the background profile. Errors have been calculated following the Narukage et al. (2011) procedure. The dotted lines bound values of the fitted profile, plus and minus the 1σ statistical uncertainty.

because the 171 Å and 284 Å filters are sensitive to different temperature regimes. The EUVI ratios are monotonic over limited temperature intervals; this fact implies that we have to select a temperature range a priori for each filter ratio. In this work, we selected 7×10^5 K $< T_{195/171} < 2 \times 10^6$ K and 1.26×10^6 K $< T_{284/195} < 2.8 \times 10^6$ K, as over these intervals the ratios are linear functions of temperature; lower temperatures are unrealistic and temperatures higher than 2.8×10^6 K correspond to temperatures too high to be compatible with our ratios and/or they would imply no emission in the 195 Å waveband, contrary to what we indeed observe.

The observed ratios have been compared with the predicted ratios of the filters, computed from the filter response functions F_i, assuming coronal abundances from Feldman (1992) and the ionization equilibrium of Mazzotta et al. (1998). We obtained a temperature profile along the jet at each time an image was acquired. Assuming a cylindrical jet shape with a cross section diameter (l) given by the width of the jet, we also calculated the jet and background CEMs and the jet electron densities (see Equation (1)). Obviously, our approach implicitly neglects out-of-equilibrium effects that might be at work in the jet plasma: these have been described in flaring loops, e.g., in the work of Bradshaw & Mason (2003). Recalculating filter responses and ratios for out-of-equilibrium plasmas is a major effort far beyond the scope of the present work. However, we call the reader's attention to this possibility and point out that non-equilibrium effects are minimized whenever jets keep a constant temperature in time and throughout their structure.

A further parameter we calculated from the XRT data analysis is the outflowing plasma speed in the jet. To infer its value, for the standard jet, we visually evaluated the height reached by the jet in images taken at different times. For the blowout jet, where we have higher temporal resolution data, we used the images within the mask adopted for the temperature/density analysis (which lies along the direction of the propagating outflow) and placed them side by side for all available images. These "stacked" intensity images build up a space-time plot (see, e.g., Sakao et al. 2007) where the intensity fronts form bright strips whose slope (angular coefficient) gives the outflow speed value.

In the next section, we present the results of our analysis.

4. RESULTS

4.1. The Standard Jet

Figure 4 shows the profiles of the *C_poly*, *Al_mesh*, and *Al_poly* filters intensities versus distance along the jet at ≈22:51 UT. In the background, the intensities over the jet area at 22:30 UT, before the occurrence of the jet, are shown. The triangles and their corresponding error bars represent average intensities over the jet width with their statistical 1σ uncertainties; the solid line is a fourth-order polynomial fit to the jet intensity data. The dotted lines bound values of the fitted profile, plus and minus the 1σ statistical uncertainties. The diamonds and the dashed line represent the background intensity and the polynomial fit to the data, respectively, while the dash-dot line indicates the jet intensity versus distance profile after the removal of the background. As long as the lower dotted jet line lies above the upper dotted background line, i.e., as long as the jet intensity is higher than the background intensity by 2σ, temperatures inferred via the filter ratio technique are statistically significant.

Temperatures derived from these data are shown in Figure 5 (left and middle panels), which shows the temperature versus distance profile for the standard jet derived from the *Al_poly/Al_mesh* and *C_poly/Al_mesh* filter ratios,
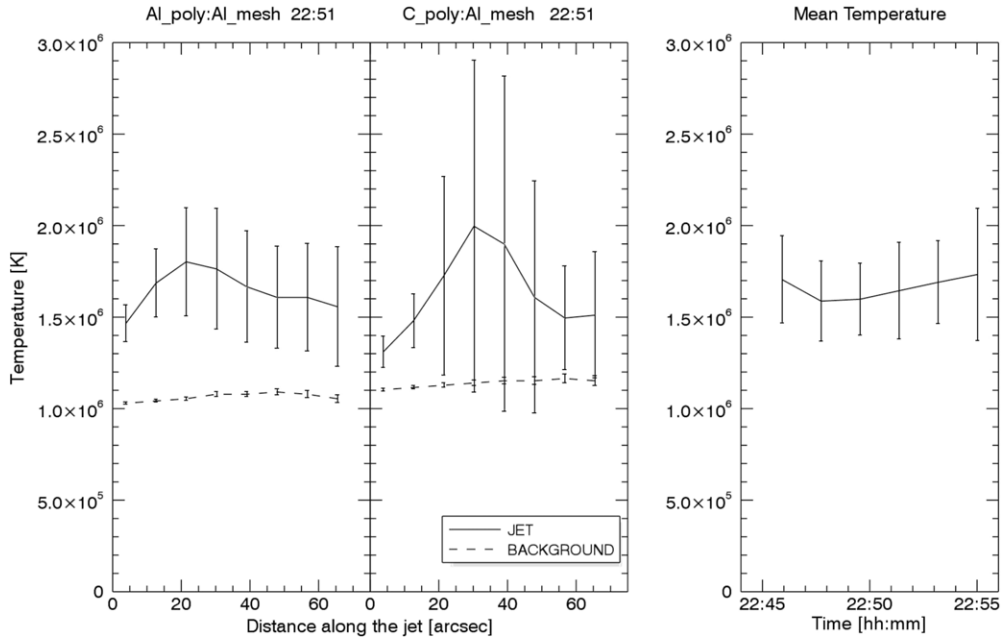
Figure 5. Plasma temperature vs. distance along the jet for the standard jet at 22:51 UT obtained from the ratio Al_poly/Al_mesh (left panel) and C_poly/Al_mesh (middle panel); distance is given in image pixels from the base of the jet. The dashed lines with (very small) error bars are the derived temperatures of the background corona. The right panel shows the profile of the temperature, averaged over the jet length, as a function of time (from the Al_poly/Al_mesh filter ratio).
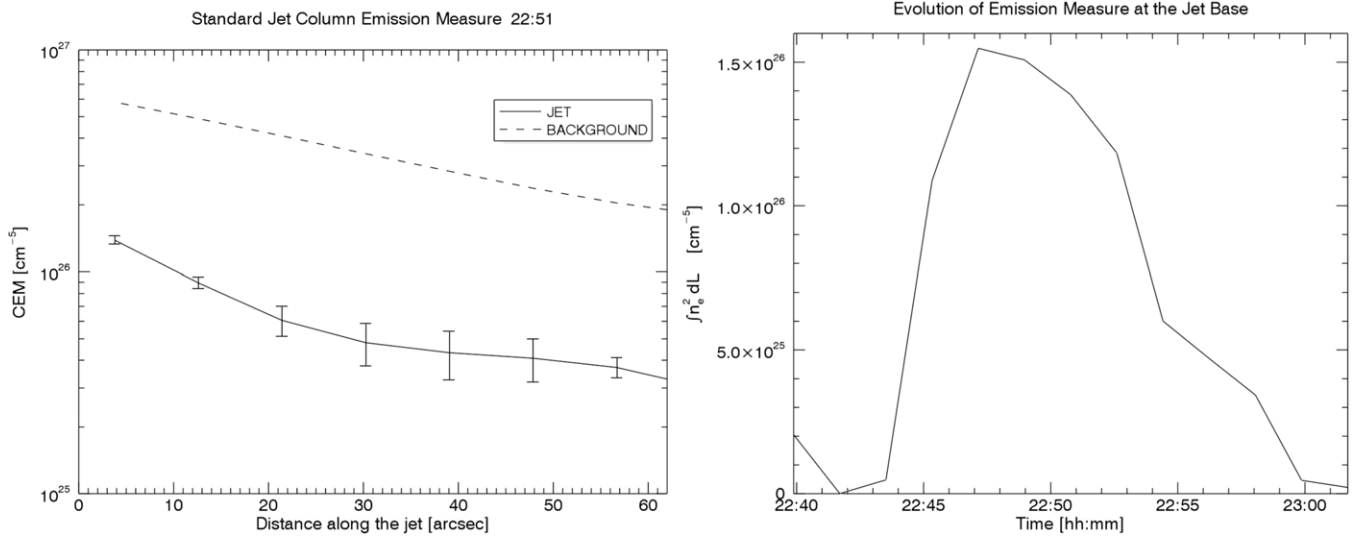

Figure 6. CEM of the standard jet vs. distance along the jet axis (left panel), inferred from the ratio Al_poly/Al_mesh at $\approx$22:51 UT. The right panel shows the profile of the base CEM vs. time over the lifetime of the jet.

respectively. The black bars represent the temperature of the jet plasma with its statistical errors, while the dashed line is the temperature of the background material. Jet temperatures from the two filter ratios are consistent within the error bars at about 1.5×10^6 K, suggesting agreement between the values of the mean temperature in the volume that has been integrated over.

The increase in the temperature error bars of the C_poly/Al_mesh ratio (middle panel) around pixels 25–50 arcsec from the jet base is due to a sudden decrease in the slope of the ratio of the filter response functions for values measured at these positions; since the error is inversely proportional to the derivative of this ratio, the error increases noticeably (see Equation (15) of Narukage et al. 2011). Hence, temperatures inferred from the Al_poly/Al_mesh ratio are more reliable than those derived from the noisier C_poly/Al_mesh ratio, although they are not inconsistent with each other. The right panel of

Figure 5 shows the profile of temperature versus time, averaged over the entire jet length, from values obtained only from the more reliable ratio. Over the examined time interval, the temperatures appear to be constant. The background coronal temperature of $\approx 1.0 \times 10^6$ K agrees with, e.g., the Doschek et al. (2010) polar CH background value.

The CEM has been inferred from Equation (1). In Figure 6, we show the profiles of the CEM versus distance along the jet, at 22:51 UT, inferred from the ratio Al_poly/Al_mesh (left panel). The solid line with error bars shows the CEM of the jet with 1σ uncertainties; errors were calculated following the procedure worked out by Narukage et al. (2011) and, in particular, we used Equations (15) and (16) of their paper. The dashed line shows the CEM for the background and foreground CH plasma. The highest CEM turns out to be at the jet base, decaying steadily with distance from the base up to about 40 arcsec, where it

stabilizes around values of 5×10^{25} cm^{-5}. The CEM of the background plasma is about one order of magnitude higher (6.5×10^{26} cm^{-5}) because of its longer LOS-integration path compared with the thickness of the jet. Figure 6 (right panel) shows that the CEM of the jet increases initially, reaching a maximum of about 2×10^{26} cm^{-5} at 22:49 UT, and later decreases, accounting for the jet disappearance in the *Al_mesh* filter at ≈23:00 UT.

If we assume a cylindrical shape for the standard jet, we can estimate the jet width along the LOS to be about 2×10^3 km and obtain a density profile for the jet plasma both along the jet and in time. Densities n_e at the time of maximum jet brightness are ≈1×10^9 cm^{-3} at the jet base and half of this value 60 arcsec above the base. Similar values have been found by several authors (e.g., Culhane et al. 2007; Doschek et al. 2010), and Doschek et al. (2010) analogously found jet densities to fall as a function of height in the data sample they studied. Our density values eventually decrease with time, accounting for the jet disappearance.

The temperatures we found are slightly higher and lower than the temperatures inferred by Nisticò et al. (2011; 0.8–1.3 × 10^6 K) and by Culhane et al. (2007; 2–3 × 10^6 K), respectively, and agree with the 1.4×10^6 K estimate of Doschek et al. (2010). Temperatures obtained by Madjarska (2011) of up to 12×10^6 K at the footpoints of a jet are not observed in our data, as they would imply ratios a factor of two to three higher than those we measure. It is possible that the energy deposition site with such a high temperature is tiny and undetectable in limb observations because of the more extended LOS of limb events with respect to disk events. On the other hand, the temperatures in Madjarska (2011) of outflowing plasmas—ranging from 0.5 to 2×10^6 K—are consistent with our results.

Because the jet is within the FOV of *STEREO A*, we made an extensive search for a signature of the event in EUVI, but while the BP shows up in all four EUVI channels, we only identify a very weak jet-like structure above the flaring BP in the 195 Å and 284 Å wavebands, with too low a count rate to allow us to evaluate temperatures from these EUVI data. In order to check whether or not the weak emission of the EUVI jet is consistent with the XRT-inferred jet physical parameters, we used the latter to calculate the expected EUVI background/jet emission ratios at about 20 arcsec above the base of the jet, taking into account the EUVI filter responses. It turns out that the ratios in the 171 Å, 195 Å, and 284 Å channels, respectively, are ⩾100, 3.6, and 2. Hence, while we obviously cannot expect to detect the jet in the 171 Å channel, we might expect the jet to be more clearly detectable in the other channels. We ascribe the weakness of the EUVI jet to the different vantage points of *Hinode* and *STEREO A* that result in a higher *STEREO* background that washes out most of the jet feature. As we will see in the next section, a similar effect occurs in the blowout jet, whose components do not always appear in both *STEREO* spacecraft.

We also derived the outflow plasma speed ((2.5 ± 0.3) × 10^2 km s^{-1}) visually from the expansion of the top of the jet. Obviously, what we measure represents only the component of the speed normal to the LOS, but because these events are within polar CHs, where the magnetic field is radial, we can assume that outflows are radially oriented.

So far, little information has been given in the literature about the spatial and temporal evolution of jet parameters. Hence, we analyzed the variation of temperature versus time and temperature versus distance along the jet. Temperature does not decrease along the jet axis; this result suggests that at any given time, the jet intensity decreases with distance only because of a density decrease. This density decrease with distance could be due in part to a funneling out of jet material into the outer solar atmosphere. The right panel of Figure 5 reveals that at least over a time interval of about 10 minutes, the temperature of the jet remains about constant; over this time interval, the jet appears to move laterally. This movement of the jet is not real, however; rather, it shows that reconnection migrates sideways with time. In other words, a sequence of jet strands brightens progressively at increasing distance from the first jet. Hence, a jet structure is maintained at a constant temperature by a shifting reconnection location that occurs progressively shifting sideways with respect to the episode that initiated the jet, but the amount of plasma that is carried upward changes with time. The lateral motion (meaning the apparent lateral motion of the jet or the shifting motion of the reconnection point) occurs at a speed ≈7 km s^{-1}, where this value is the projected speed on the plane of the sky. This value is in agreement with predictions from the Moreno-Insertis et al. (2008) model. The Pariat et al. (2009) model suggests that the lateral shift occurs at a speed of one-fifth to one-tenth of the upward plasma speed along the jet axis; this fact would imply that projection effects lead us to underestimate the speed at which reconnection migrates laterally. Because the jet occurs in polar regions, we lack a magnetic field map that would allow us to make a more realistic estimate of the speed at which reconnection moves laterally and ascertain whether our lateral speed could take a higher value than we estimated.

The open question of whether the jet plasma escapes from the solar gravitational field can be addressed with the help of data from COR1, the coronagraph on board the *STEREO* missions. However, we did not find any evidence of the jet in COR1 data.

4.2. The Blowout Jet

Because *Hinode*/XRT acquired images of the blowout jet only in the *Al_poly* filter, we determined the jet temperature applying the filter ratio technique only to EUVI data. The jet area was imaged in all EUVI channels of *STEREO A* and *B*, as shown in Figure 7. The top and bottom panels show simultaneous images of the blowout jet acquired at 12:06 UT, on 2007 November 3, by, respectively, *STEREO A* and *B*, at 171 Å (left panel), 195 Å (middle-left panel), 284 Å (middle-right panel), and 304 Å (right panel). The occurrence of the jet in the 304 Å channel is a key signature of blowout jets (Moore et al. 2010, 2013) and hints at a blowout eruption of the base arch.

The composite multi-strand structure of the blowout shows up clearly: in particular, in the 195 Å images, we identify three different strands, each of which reaches a different altitude. In the following, we illustrate results from the temperature analysis of the three substructures of the jet, which we refer to as Strand1, Strand2, and Strand3, from right to left. We notice that the strands are not always visible in both spacecraft: for instance, Strand3 does not show up in the 171 Å images of *STEREO A*, while it shows up clearly in the *STEREO B* images. Because strands are not always seen by the two spacecraft, we cannot say whether different strands come in a variety of intensities and lengths or whether the differences we observe depend on the viewing angle or on the evolutionary stages jets go through over their lifetime that are randomly sampled in our images. We surmise that the background emission of the ambient corona, originating from different pathways in the two spacecraft, affects the visibility of the strands; we have already observed this fact for the standard jet.
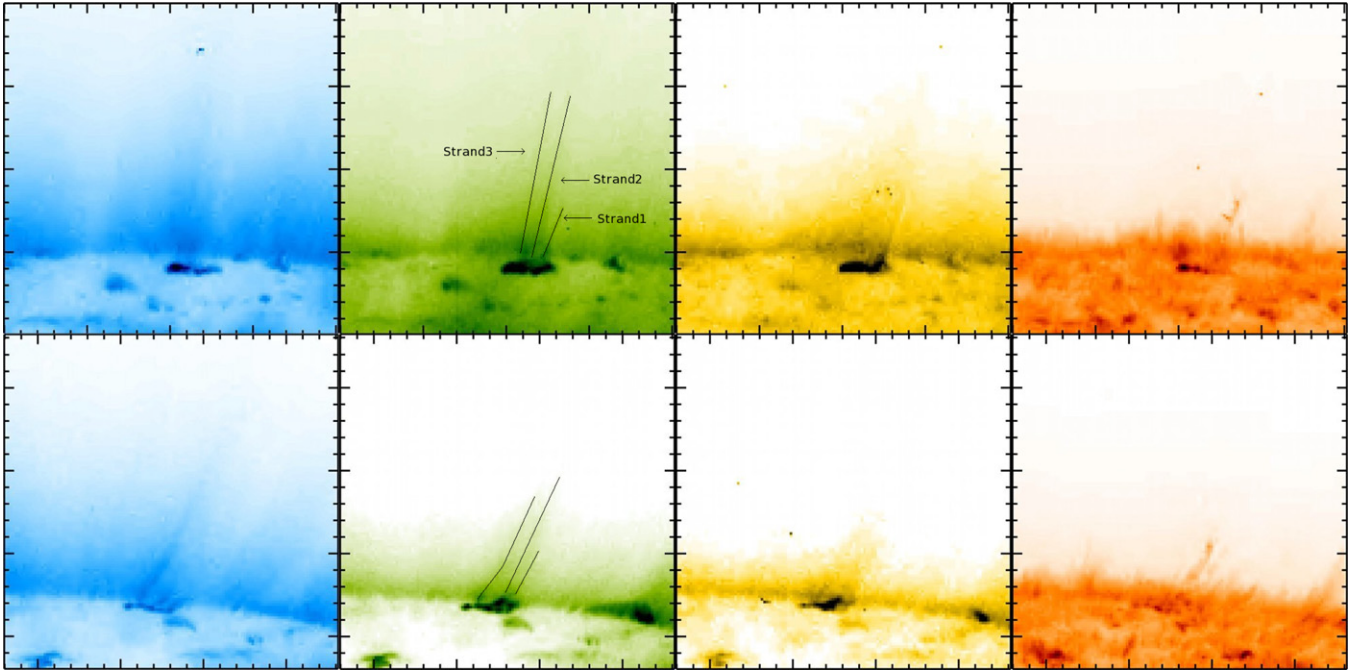
Figure 7. Images of the blowout jet of 2007 November 3, acquired by the EUVI telescopes on board *STEREO A* (upper panels) and *STEREO B* (lower panels) at 12:06 UT in (from left to right) the 171, 195, 284, and 304 Å channels.

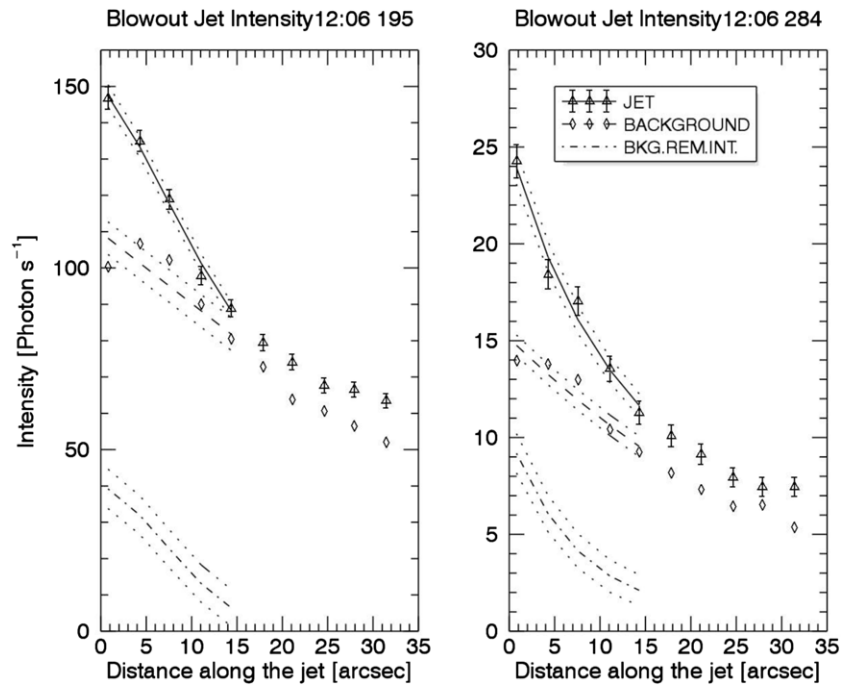(A color version of this figure is available in the online journal.)

Figure 8. Profile of the intensity (photon s^{-1}) vs. distance along the axis of Strand1 of the blowout jet in the 195 Å (left panel) and 284 Å (right panel) channels of EUVI *A*, at 12:06 UT on 2007 November 3. See the caption of Figure 4 for other notations.

Figure 8 shows the intensity (photon s^{-1}) along the axis of Strand1 at 12:06 UT, as measured in the 195 Å and 284 Å channels of *STEREO A*/EUVI, with error bars. The background emission and the jet intensity after the background subtraction are also shown. In the 171 Å channel, the jet emission does not exceed the background intensity; hence, the 171 Å image is not shown and temperatures have been inferred via the 284 Å/195 Å filter ratio only.

Figure 9 shows the 284 Å/195 Å temperature of Strand1, from data of the *STEREO A*/EUVI package. The temperature profile

is characterized by higher values than found in the standard jet, with values around 2×10^6 K. Because EUVI collects a larger number of photons than *Hinode*/XRT, the 1σ error bars are smaller in these EUVI plots. Temperatures inferred from *STEREO B* range between 1.8 and 2×10^6 K and are nearly constant over a height interval of $\approx$12 arcsec.

The CEM of Strand1 is shown in Figure 10 and is quite similar to that of the standard jet: as for the standard jet, we point out that the background CEM is much higher than that of the jet. The densities inferred from the CEM show an almost
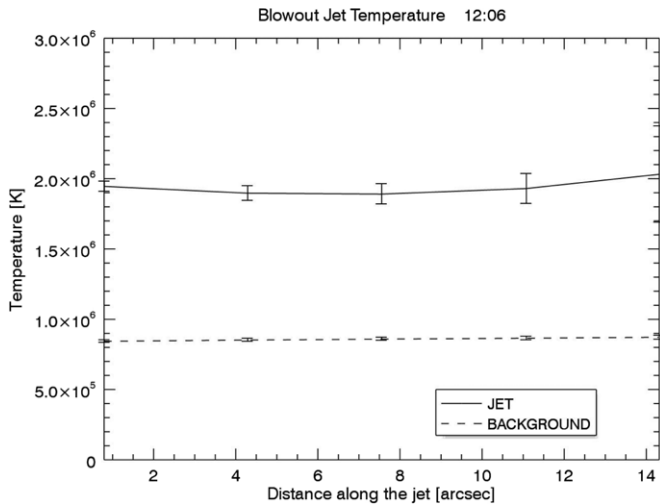
Figure 9. Temperature vs. distance profile for blowout jet Strand1, at 12:06 UT, from the 284 Å/195 Å filter ratio calculated from data acquired by EUVI telescopes on *STEREO A*.
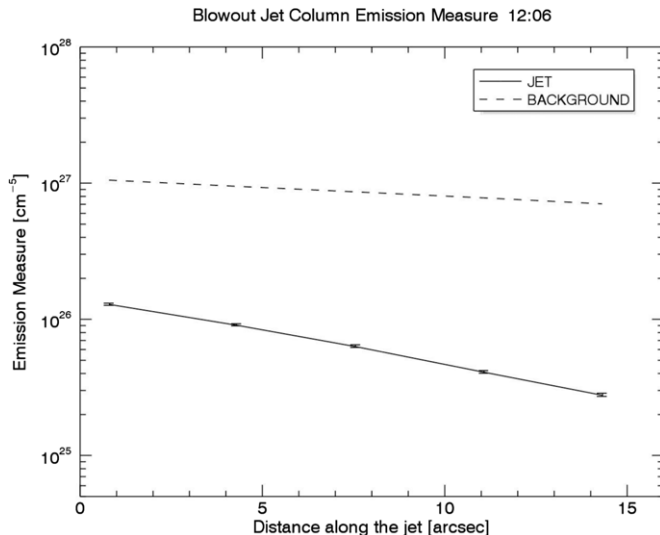

Figure 10. CEM for Strand1 of the blowout event, from temperatures inferred from the ratio 284 Å/195 Å. *STEREO A* data have been used, as in Figures 8 and 9.

linear decay from the jet base to 15″ above the base, decreasing from 8×10^8 cm^{-3} to 3×10^8 to cm^{-3}. These values are slightly lower than those of the standard jet. These values, however, were obtained at a time (12:06 UT) that was one or two minutes prior to the probable maximum brightness in soft X-rays, based on the XRT data; whether the densities would have been higher at the time of maximum soft X-ray brightness is unclear. The same procedure, applied to *STEREO B* data, yields comparable density values, decreasing from 6×10^8 cm^{-3} to 2.8×10^8 cm^{-3}, over the same height interval (although we cannot establish an absolute scale for distances along the jet axis as seen by the two spacecraft). We also examined the other strands of the blowout: the temperatures of Strand2 and Strand3, independent of whether they are evaluated using *STEREO A* or *STEREO B* data, are $1.8–2 \times 10^6$ K. In particular, Strand2, which can be followed over 60 arcsec, maintains a constant temperature throughout its length. Densities are similarly within the values reported above for Strand1.

As mentioned in Section 3, we used stacked intensity plots to obtain the outflow speed of blowout jet plasma from the XRT *Al_poly* data that have a time resolution of 40 s. It is easy
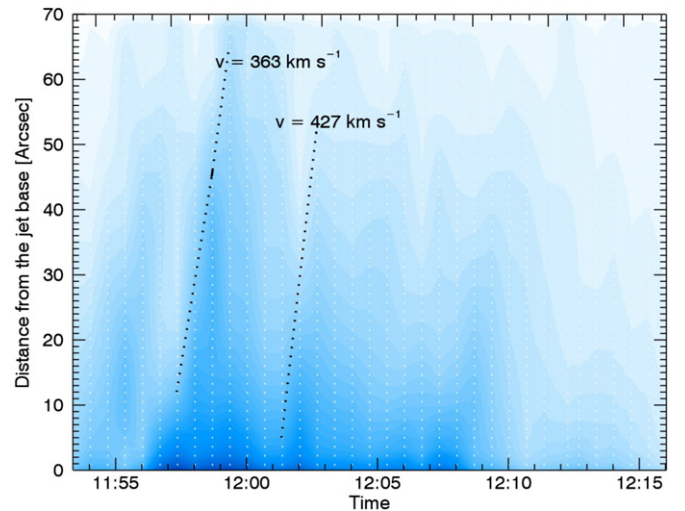

Figure 11. Stacked plot for the Strand2 structure of the blowout jet. The superposed black dotted lines are trajectories of the jet intensity fronts. The inferred plasma outflow speed is also given. The vertical white dotted lines give the times that individual frames were acquired.

(A color version of this figure is available in the online journal.)

to identify the three strands observed by *STEREO A* and *B* in the XRT images, which provide a view from a vantage point in between the *STEREO* spacecraft. Figure 11 shows the time-distance plot of Strand2, chosen because it has a longer duration than the other strands. Also, to enhance the visibility of the *Al_poly* intensity fronts, an unsharp mask technique has been applied to the data. The dotted lines outline the intensity-front trajectory along the jet axis. The shape of the intensity fronts at lower altitudes shows that the plasma accelerates from ≈100 to ≈350–400 km s^{-1} over the first one to two minutes after jet initiation, reaching a higher speed than inferred for the standard jet. We point out that the long time cadence at which the XRT images of the blowout have been acquired (40 s) would allow us to measure speeds as high as ≈1000 km s^{-1}.

It is interesting to compare outflow speeds inferred from this technique with values inferred via a completely different method. Patsourakos et al. (2008) first made a three-dimensional reconstruction of the trajectory of a jet they observed and then computed the plasma outflow speed from the distance versus time plot of the jet front. These authors found that a phase about 30 minutes long where the jet rose at 10–20 km s^{-1} is followed by an acceleration phase where the average outflow speed (over ≈2 minutes) is on the order of 90 km s^{-1} and rises subsequently to a speed of ≈300 km s^{-1}. The initially lower value, and the terminal speed of ≈300 km s^{-1}, are consistent with the values we found from stacking plots. In the view of Patsourakos et al. (2008), these speeds correspond to the untwisting of the flux tube followed by a nearly vertical rise. This scenario may apply to our observations as well.

Figure 11 provides evidence for the occurrence of repeating jets, three to five of them in this case, that repeat at a time interval of ≈300 s. This behavior is not unusual: repetitive plasma outflows have been noted by Scullion et al. (2009; although with a far different periodicity than we find here), while Morton et al. (2012) detected multiple bright ejections in time-distance plots from cross-cuts along/through a blowout jet and jet-related phenomena observed by *SDO*/AIA. *SDO*/AIA data have also been used by Liu et al. (2011) in their analysis of a standard-to-blowout jet where analogously no fewer than 10 plasma blobs
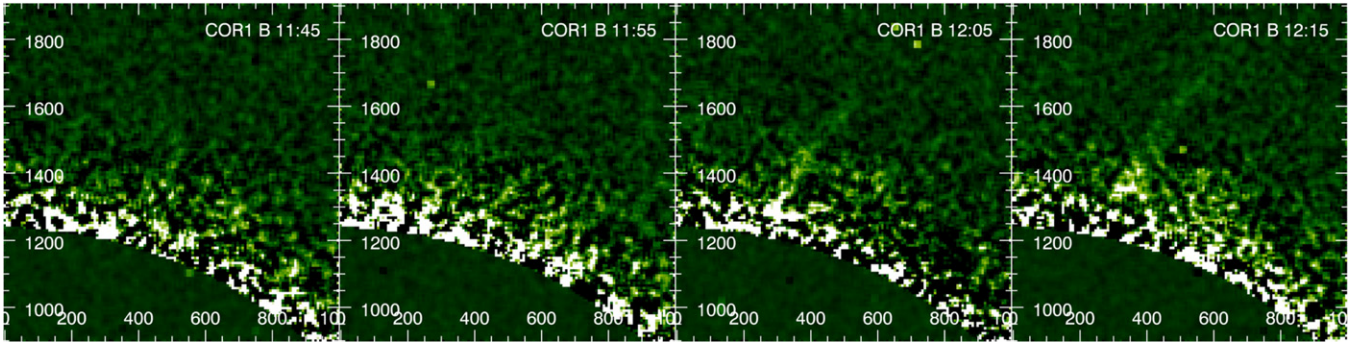
Figure 12. Sequence of running difference images from the COR1 coronagraph on board the *STEREO B* satellite, showing the blowout jet reaching altitudes $\geqslant 1.4$ solar radii.

(A color version of this figure is available in the online journal.)

streaming outward were detected. Although the interpretation of these results is not easy, and further data are needed, it is likely that the observed phenomena point to repetitive reconnection events between closed and open field lines.

The data of the standard jet have a lower temporal resolution comparable with that of the blowout jet data (110 s versus 40 s). Furthermore, the lower quality time–distance stacked plot for the standard jet (not shown here) provides values of the outflow speed that are consistent with the values obtained visually. Furthermore, this stacked plot supports the occurrence of repetitive ejection episodes within the standard jet as well. The present analysis implies that this behavior may be shared by both the standard and the blowout jets.

As with the standard jet, we searched COR1 data for evidence of the blowout jet. Figure 12 shows four frames of polarized brightness of the solar corona as observed by the COR1 instrument on board the *STEREO B* mission. These are running difference images, smoothed to reduce the noise. The jet is clearly visible in the COR1 FOV reaching $1.8 R_{\rm sun}$ at 12:05 UT. This observation is consistent with an ejection that occurs at 11:55 UT and propagated upward, accelerating beyond the $400 \ {\rm km \ s^{-1}}$ we estimated from the XRT images and eventually overcoming the solar gravitational field to be fully ejected from the Sun.

5. ENERGY BUDGET

In a scenario where jets originate because of a reconnection event triggered by flux emergence within an open ambient field, we may check whether or not standard/blowout jets imply any difference in the magnetic energy release that fueled them. In the following, we try to estimate, although crudely, the energy components that contribute to the energy budget of the ejections. We assume that reconnection occurs at the base of the jet, possibly slightly above the bright points base, at an altitude of the order of 5–10 arcsec. We furthermore assume that the magnetic energy is converted into kinetic, potential, work, wave (Alfvén), and radiative energy. We ignore conduction along field lines, as jets maintain a constant temperature along their axis, and we ignore the fraction of energy that is dissipated downward with respect to the reconnection site (likely of the same order of magnitude as that released upward).

Hence, the magnetic energy flux ($F_{\rm rec}$, erg cm^{-2} s^{-1}) that is released, per event, is distributed between the enthalpy $F_{\rm enth}$, wave F_w, kinetic $F_{\rm kin}$, potential $F_{\rm pot}$, and radiative $F_{\rm rad}$ energy fluxes:

$$F_{\rm rec} = F_{\rm enth} + F_w + F_{\rm kin} + F_{\rm pot} + F_{\rm rad}, \qquad (3)$$

where

$$F_{\rm enth} = \frac{\gamma}{\gamma - 1} p v \qquad (4)$$

$$F_w = \sqrt{\frac{\rho}{4\pi}} \xi^2 B \qquad (5)$$

$$F_{\rm kin} = 1/2 \rho v^3 \qquad (6)$$

$$F_{\rm pot} = \rho g L v \qquad (7)$$

$$F_{\rm rad} = n_e n_{\rm H} \chi T^\alpha L, \qquad (8)$$

where p, ρ, g, and γ are, respectively, the plasma pressure, the mass density, the gravity, and the ratio of the specific heats ($\gamma = 5/3$). n_e is the plasma number density ($n_{\rm H} = n_e$), ξ is the amplitude of unresolved non-thermal plasma motion, B is the field strength, and L is the vertical extension of the jet. For $F_{\rm rad}$, we adopted the analytic approximation and the values of α; χ is given by Rosner et al. (1978; $\alpha = 0$, $\chi = 10^{-34.94}$, with χT^α in W m^3).

The wave energy flux is supposed to be due to waves generated at the time of reconnection when field lines change shape to relax to their final configuration. Evidence for Alfvénic waves in jets has been found by, e.g., Cirtain et al. (2007), who reported a physical displacement of the jet axis. Because we do not observe any recursive lateral shift of the jets that may hint at the wave amplitude, we make no hypothesis about the nature of excited waves and we only assume that waves appear as unresolved plasma motions broadening spectral lines and that they propagate at the Alfvén speed. The wave amplitude ($\xi = 100 \ {\rm km \ s^{-1}}$) is assumed to be the value given in Kim et al. (2007) who, from EIS data, found non-thermal velocities ranging from 57 to 106 km s^{-1} at the footpoints of jets. This result is also consistent with observations of Scullion et al. (2009) that pointed out that large jet outflows are associated with regions of large line broadening. As we do not have any information about the differences in the wave flux between the two jet families, we assume F_w has the same value in the standard and blowout jets. For the field strength, B, we assume that outflows occur at approximately the local Alfvén speed, v_A ($v_A = B/\sqrt{4\pi\rho}$), and infer the magnetic field strength from this hypothesis. We point out that we likely underestimate the magnetic field strength as the bulk flows do not necessarily have the same Alfvén speed as the small-scale reconnection flows that originate in the diffusion region. This assumption yields magnetic field strengths of ≈ 2.8 G and 4.5 G for the standard and the blowout event, respectively.

Table 1
Physical Parameters of the Jets

	Standard Jet	Blowout Jet
T_e	1.6×10^6 K	1.8–2×10^6 K
CEM	8×10^{25} cm^{-5}	1×10^{26} cm^{-5}
n_e	6×10^8 cm^{-3}	6×10^8 cm^{-3}
B	2.8 G	4.5 G
v	250 km s^{-1}	400 km s^{-1}

In Table 1, we show the values of the parameters we used for evaluating the energy fluxes of the standard and blowout events; these parameters are representative of what we measured over the duration and along the jets we analyzed. The magnetic field strengths listed in Table 1 correspond to the guesses we made about values in the reconnection region and not to the values of the field in the BP region where the jets originate.

Because the kinetic energy flux depends strongly on the outflow speed, its value for the blowout jet ($\approx 3 \times 10^7$ erg cm^{-2} s^{-1}) is larger by about a factor of four than that of the kinetic energy flux of standard events, while the blowout enthalpy flux ($\approx 1.7 \times 10^7$ erg cm^{-2} s^{-1}) is 1.6 times larger than the enthalpy flux of the standard jet. These are the forms of energy where most of the energy flux dissipates, while the other energy fluxes are about one order of magnitude lower (the radiative energy flux is negligible; the potential and wave energy fluxes are, in the standard versus the blowout eruptions, 2.5×10^6 and 2.5×10^6 versus 4×10^6 and 4×10^6 erg cm^{-2} s^{-1}, respectively.).

Hence, the energy released by reconnection is nearly three times as large in the blowout jet as in the standard jet. However, if we take into account the multiple strands that show up in our blowout event, we can say that fueling a blowout requires 10 times as much energy as is needed to fuel our standard ejection. Altogether, the energy that goes into a blowout jet is on the order of 2×10^{27} erg.

However, so far, we have neglected the cool component that appears in blowout jets and in our jet shows up in the COR1 images of Figure 12. Indeed, these jets are considered to be miniature versions of two-ribbon flares and although an estimate of the mass of the CMEs associated with these events is still missing, a blowout CME has been recently observed by Shen et al. (2012) in *SDO* data, confirming that these ejections are the low energy representatives of this class of flares. Two ribbon flares are the most energetic flares: the global energetics of 38 eruptive events have been evaluated by Emslie et al. (2012), who concluded that most of the energy of these events resides in the kinetic energy of the associated CME (of the order of a few times 10^{32} erg). Hence, it becomes mandatory to estimate the energy content of the CME associated with our blowout event. Although the COR1 images reveal the cool component associated with the blowout we examine, we have no evidence of a CME, most likely because its size and/or density is too low to be revealed by *STEREO* or *SOHO* experiments and we have to resort to an indirect technique to guess its mass.

Yashiro & Gopaslwamy (2009) reported a statistical relationship between the X-ray fluence in the 1–8 Å band of solar flares and the kinetic energy of the CME associated with the flare. Drake et al. (2013) applied this relationship to ejections from active stars, possibly brighter than the Sun by a factor of the order of 1000, assuming that the relationship holds over a wide range of CMEs and flares. Here, we make the same assumption and extrapolate the Yashiro & Gopaslwamy (2009) relationship to smaller events, known, as we said, to be the small-scale analogs of large events.

The X-ray emission of blowout jets can be estimated from their physical parameters, typical sizes, and lifetimes. The emission turns out to be slightly lower than 10^{26} erg, two to three order of magnitudes lower than the X-ray emission of the flares examined by Yashiro & Gopaslwamy (2009). Adopting the fit to their data given by Drake et al. (2013) in their Figure 1, it turns out that the mass of the CMEs associated with weakly X-ray emitting flares is on the order of 10^{12} g, that is, on the order of 1/1000 of the average mass of CMEs. This mass compares well with the mass of CMEs given in the LASCO catalog, where the smallest events have a mass of about 10^{13} g, accounting for their lack of visibility in the *SOHO*/LASCO coronagraphs.

Once the mass of the CME associated with our jet is known, we can estimate its kinetic and potential energy, which turn out to be on the order of 10^{27} erg. Hence, adding the energy residing in the cool component to the hot component energy of the blowout results in a total energy of the order of 10^{27} to 10^{28} erg, making this total energy budget larger than that of standard events by about a factor of 20–30. Hence, blowouts are typically 10^5 times less energetic than the largest solar eruptions, which are known to emit about 10^{32-33} erg.

We note that the overall energy released by reconnection over our jets' lifetimes does not entirely go into feeding the ejections, as the jets are rooted in BPs whose intensity increases noticeably over the duration of the jets. This fact is especially true in the blowout event, where a large area undergoes a major brightness increase. This brightness increase points to an even larger energy release in blowout jets than we estimated above on the basis of impulsive ejections only.

The estimates we give are obviously a crude approximation of the more rigorous estimates that might be obtained if, for instance, waves would be detected, CMEs could be observed, magnetic fields could be measured, and outflow speeds could be more accurately evaluated. When dealing with such small ejections, we are at present in the situation that we have been in for years in which the energy budgets of large flares, as we mentioned, are only recently being correctly calculated (Emslie et al. 2012). However, we deem it interesting to have an even rough assessment of the jets' energy budgets to be used by modelers and theoreticians as an observational reference. The most uncertain term in the estimate of the energy budget is the wave term F_w: for instance, the magnetic field B may be higher than we estimated, resulting in a higher wave flux. Also, we may have mistakenly used the Alfvén speed calculating F_w. However, it is unlikely that the error we made is higher than a factor three to four, which will leave our conclusions practically unchanged. Another source of uncertainties may reside in the wave amplitude estimate and in the evaluation of the outflowing plasma speed from the stacking plots, which are not easily interpreted. In their analysis of a polar jet observed by the *SDO*/AIA assembly, Shen et al. (2012) give a total estimate of the jet energy on the order of 2×10^{29} erg. This value is consistent with the value given here, if we consider that Shen et al. (2012) arbitrarily assume the electron density to be 4×10^9 cm^{-3}, nearly one order of magnitude larger than the electron density of our events. We note, however, that these authors study a jet that falls back to the Sun, and thus the properties of their event may not be the same as those of the jet analyzed in this work.

6. SUMMARY AND CONCLUSIONS

In this work, we aimed at inferring differences in the physical parameters of two solar X-ray jets, one each from two previously identified families of CH X-ray jets, standard jets and blowout

jets. Apart from the multi-components that characterize the blowout jet, our analysis has shown that with respect to our standard jet, our blowout jet has (1) possibly an electron temperature higher by 10%–20% (although the difference in the temperature of the two jets is marginally above the statistical error and further analysis is required to resolve this issue) and, (2) an outflow speed higher by ≈a factor 1.6. We note in passing that the temperatures and densities we inferred are in agreement with predictions from a model by Pariat et al. (2009), which gives a temperature of 1.7×10^6 K and a density of 2×10^{-16} g cm^{-3}. Also, we found (3) that the energy dissipated by reconnection that fuels the blowout jet is about one order of magnitude larger than the energy that feeds our standard jet.

On the basis of our sample of one object from each category, these properties suggest that blowout jets, rather than standard jets, originate from the stronger magnetic field regions within CHs. This result might suggest that jets that escape into the heliosphere are likely to belong to the blowout category, in agreement with results from our COR1 analysis (although we cannot rule out the possibility that standard jets also escape into the heliosphere, but do not have a high enough emission measure to be detected). Should this case be true, we nevertheless have shown in Pucci et al. (2013) that the contribution of these jets to the solar wind mass loading is likely to be negligible. The same can be said about the energy they feed to the corona, which is about a factor 10^4 smaller than that required to maintain the corona and solar wind. If blowout jets are accompanied by other features, such as type II spicules, as suggested by Moore et al. (2010) and Sterling et al. (2010), these figures may possibly change, but an analysis of this scenario is beyond the scope of the present investigation.

The stacked plot of the blowout jet (Figure 11) reveals the occurrence of multiple reconnection events. We find the same behavior from a visual analysis of the standard event: both plots indicate the occurrence of multiple reconnection episodes. This fact is also confirmed by the BP where the jets originate, whose brightness undergoes significant enhancements associated with each jet episode. Variations of the BP intensities have been observed by, e.g., Chandrashekhar et al. (2013), who also interpreted these variations as being generated by repeated reconnection episodes. Hence, while there is little doubt that reconnection dictates the observed changes in BPs and generates the jets, it is hard to say whether the stacked plots of standard and blowout jets have a unique interpretation. In blowout jets, we know that reconnection occurs at different places within the BP; hence, the repeated blobs we image in individual strands may be indicative of bursty reconnection and may be analogous to blobs observed in current sheets identified in large CME events (see, e.g., Lin et al. 2005; Schettino et al. 2009; Riley et al. 2007). In this case, the stacked plot of individual blowout jet strands would be consistent with, e.g., time-dependent Petschek reconnection (Priest & Forbes 2000) occurring in the current sheet associated with these ejections. This interpretation is especially appealing, as it is believed that blowouts are miniature representations of large CMEs (see, e.g., Liu et al. 2011). On the other hand, the drift of standard jets and the associated stacked plots would be indicative of a reconnection region migrating to different flux surfaces, as implied in, e.g., the Pariat et al. (2009) model.

REFERENCES

Bradshaw, S. J., & Mason, H. E. 2003, A&A, 407, 1127
Chandrashekhar, K., Krishna Prasad, S., Banerjee, D., Ravindra, B., & Seaton, D. B. 2013, SoPh, 286, 125
Chen, H.-D., Zhang, J., & Ma, S.-L. 2012, RAA, 12, 573
Cirtain, J. W., Golub, L., Lundquist, L., et al. 2007, Sci, 318, 1580
Culhane, L., Harra, L. K., Baker, D., et al. 2007, PASJ, 59, 751
Doschek, G. A., Landi, E., Warren, H. P., & Harra, L. K. 2010, ApJ, 710, 1806
Drake, J. J., Cohen, O., Yashiro, S., & Gopalswamy, N. 2013, ApJ, 764, 170
Emslie, A. G., Dennis, B. R., Shin, A. Y., et al. 2012, ApJ, 759, 71
Feldman, U. 1992, PhyS, 46, 202
Golub, L., Deluca, E., Austin, G., et al. 2007, SoPh, 243, 63
Howard, R. A., Moses, J. D., Vourlidas, A., et al. 2008, SSRv, 136, 67
Kaiser, M. L., Kucera, T. A., Davila, J. M., et al. 2008, SSRv, 136, 5
Kano, R., Hara, H., Shimojo, M., et al. 2004, in ASP Conf. Ser. 325, The Solar-B Mission and the Forefront of Solar Physics, ed. T. Sakurai & T. Sekii (San Francisco, CA: ASP), 15
Kim, Y.-H., Moon, Y.-J., Park, Y.-D., et al. 2007, PASJ, 59, S763
Lemen, J. R., Title, A. M., Akin, D. J., et al. 2011, SoPh, 275, 17
Lin, J., Ko, Y.-K., Sui, L., et al. 2005, ApJ, 622, 1251
Liu, C. L., Liu, R., Ugarte-Urra, I., Wang, S., & Wang, H. 2011, ApJL, 735, L18
Madjarska, M. S. 2011, A&A, 526, A19
Mazzotta, P., Mazzitelli, G., Colafrancesco, S., & Vittorio, N. 1998, A&AS, 133, 403
Moore, R. L., Cirtain, J. W., Sterling, A. C., & Falconer, D. A. 2010, ApJ, 720, 757
Moore, R. L., Sterling, A. C., Falconer, D. A., & Robe, D. 2013, ApJ, 769, 134
Moreno-Insertis, F., Galsgaard, K., & Ugarte-Urra, I. 2008, ApJL, 673, L211
Morton, R. J., Srivastava, A. K., & Erdelyi, R. 2012, A&A, 542, A70
Narukage, N., Sakao, T., Kano, R., et al. 2011, SoPh, 269, 169
Nisticò, G., Patsourakos, S., Bothmer, V., & Zimbardo, G. 2011, AdSpR, 48, 1490
Pariat, E., Antiochos, S. K., & DeVore, C. R. 2009, ApJ, 691, 61
Patsourakos, P., Pariat, E., Vourlidas, A., Antiochos, S. K., & Welser, J. P. 2008, ApJL, 680, L73
Priest, E. R., & Forbes, T. G. 2000, in Magnetic Reconnection: MHD Theory and Applications (New York: Cambridge Univ. Press)
Pucci, S., Poletto, G., Sterling, A. C., & Romoli, M. 2013, in AIP Conf. Proc. 1539, Solar Wind 13, ed. G. P. Zank, J. Borovsky, R. Bruno et al. (Melville, NY: AIP), 62
Riley, P., Lionello, R., Mikić, Z., et al. 2007, ApJ, 655, 591
Rosner, R., Tucker, W. H., & Vaiana, G. S. 1978, ApJ, 220, 643
Sakao, T., Kano, R., Narukage, N., et al. 2007, Sci, 318, 1585
Savcheva, A., Cirtain, J., Deluca, E. E., et al. 2007, PASJ, 59, 771
Schettino, G., Poletto, G., & Romoli, M. 2009, ApJ, 697, 72
Scullion, E., Popescu, M. D., Banerjee, D., Doyle, J. G., & Erdeĺyi, R. 2009, ApJ, 704, 1385
Shen, Y., Liu, Y., Su, J., & Deng, Y. 2012, ApJ, 745, 164
Shibata, K., Ishido, Y., Acton, L. W., et al. 1992, PASJ, 44, L173
Sterling, A. C., Harra, L. K., & Moore, R. L. 2010, ApJ, 722, 1644
Welser, J.-P., Lemen, J. R., Tarbell, T. D., et al. 2004, Proc. SPIE, 5171, 111
Yashiro, S., & Gopalswamy, N. 2009, in IAU Symp. 257, Universal Heliophysical Processes, ed. N. Gopalswamy & D. F. Webb (Cambridge: Cambridge Univ. Press), 233